

Parallel Statistical Multi-resolution Estimation

Jan Lebert¹, Lutz Künneke¹, Johannes Hagemann² and Stephan C. Kramer^{*3}

¹University of Göttingen, Department of Physics,
Friedrich-Hund-Platz 1, 37077, Göttingen

²University of Göttingen, Institute of X-ray Physics,
Friedrich-Hund-Platz 1, 37077, Göttingen

³Max-Planck-Institut of Biophysical Chemistry, Laboratory of
Cellular Dynamics, Am Faßberg 11, 37077 Göttingen

June 8, 2021

Abstract

We discuss several strategies to implement Dykstra's projection algorithm on NVIDIA's compute unified device architecture (CUDA). Dykstra's algorithm is the central step in and the computationally most expensive part of statistical multi-resolution methods. It projects a given vector onto the intersection of convex sets. Compared with a CPU implementation our CUDA implementation is one order of magnitude faster. For a further speed up and to reduce memory consumption we have developed a new variant, which we call *incomplete Dykstra's algorithm*. Implemented in CUDA it is one order of magnitude faster than the CUDA implementation of the standard Dykstra algorithm.

As sample application we discuss using the incomplete Dykstra's algorithm as preprocessor for the recently developed super-resolution optical fluctuation imaging (SOFI) method (Dertinger et al. 2009). We show that statistical multi-resolution estimation can enhance the resolution improvement of the plain SOFI algorithm just as the Fourier-reweighting of SOFI. The results are compared in terms of their power spectrum and their Fourier ring correlation (Saxton and Baumeister 1982). The Fourier ring correlation indicates that the resolution for typical second order SOFI images can be improved by about 30%.

*stephan.kramer@mpibpc.mpg.de

Our results show that a careful parallelization of Dykstra's algorithm enables its use in large-scale statistical multi-resolution analyses.

1 Introduction

An important topic in image analysis is the rejection of noise and blur from digital images. A particular example is denoising and deblurring of micrographs in optical microscopy. The unknown signal from object space is convolved with the point spread function (PSF) of the imaging apparatus and disturbed by Poissonian noise. Digital image recording leads to a projection of the convolved signal onto a discrete set of points in space (pixels) and intensities, such that the micrograph is a vector of real data of finite length. The blur operator representing the PSF is ill-posed (Vogel 2002) which makes its inversion in presence of noise a numerically expensive and difficult task. Regularization techniques have to be applied, see for example (Facciolo et al. 2009). Although the usage of a regularization term stabilizes iterative reconstruction algorithms, a regularization parameter has to be introduced, the choice of which is crucial for the estimator quality. An inadequate choice of the regularization parameter leads to either a loss of details in the image, or to artifacts from the ill-conditioned nature of the inversion problem. There are methods to choose the regularization in a spatially adaptive, iterative manner (Chen et al. 2006; Grasmair 2009; Dong, Hintermüller, and Rincon-Camacho 2011). Spatially adaptive regularization methods detect areas of under- and over-regularization in an image and then locally adapt the regularization parameter. Despite the success of these methods (Rodríguez 2013), the influence of the regularization parameter on the expected closeness of estimator to the true unknown signal is often not obvious.

A slightly different approach to the problem is given by statistical multi-resolution estimators (SMRE) (Frick, Marnitz, and Munk 2012; Frick, Marnitz, and Munk 2013). Common SMRE methods attempt to control the statistical behavior of residuals on several scales simultaneously, thus allowing the reconstruction of image details on different length scales at the same time. Figure 1 illustrates the idea. The result is equivalent to a maximum-likelihood estimator

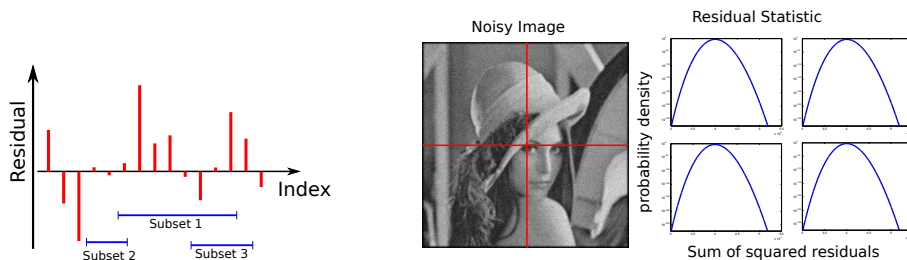


Figure 1: Left: The main concept of statistical multi-resolution estimation. The residual statistics are considered in, possibly overlapping, subsets. The distribution of residuals in each subset is required to be a realization of a given statistical process, i.e. Poisson or Gauss, with chosen confidence α . Right: Multi-resolution adapted to images. The subsets are parts of the image. The sum of squared residuals are required, in the example of normal distributed residuals, to follow a χ^2 distribution.

with a properly chosen regularization parameter (Chambolle and Lions 1997).

The appealing feature of an SMRE is that the only free parameter in the

resulting algorithm is the desired confidence level α in the hypothesis tests. Hence, the choice for the value of α has a sound statistical interpretation.

However, this comes at the price of an increased computational effort. The SMRE is to be computed iteratively. In each iteration the residuals are to be controlled in each subset of the image, see for example one of the algorithms given in (Frick, Marnitz, and Munk 2013).

A common method to minimize a convex functional with respect to a set of independent variables in presence of constraints is the alternating direction method of multipliers (ADMM) (Gabay and Mercier 1976; Hong and Luo 2012). One step in the ADMM is the projection of a given realization of residuals onto the allowed subset of residuals in \mathbb{R}^n . Because of the nature of the constraints this is the projection onto the intersection of many convex sets in Euclidean space. Each set is given by one length scale. A solution to this task is given by Dykstra's projection algorithm (Dykstra 1983; Gaffke and Mathar 1989), which projects a given noise estimate onto the feasible set of the multi-resolution constraint. A serial implementation of this algorithm is straightforward but becomes infeasible as the number of considered scales increases.

In recent years graphics cards have evolved from simple, dedicated graphics processing units (GPU) to autonomous parallel compute devices within a computer, usually referred to as general-purpose GPUs (GPGPUs). With the introduction of CUDA (compute unified device architecture) and OpenCL there are powerful, yet sufficiently simple APIs (application programming interfaces) available for parallel computing.

This work presents two different parallel implementations of Dykstra's algorithm optimized for NVidia's CUDA (Buck 2007). The first one implements Dykstra's algorithm in a general form. The second implementation emerged from the work on the first one and introduces a variant which we call *incomplete Dykstra's algorithm* (ICD). Its key feature is that only those subsets are chosen which fulfill the constraints of memory accesses on CUDA devices, i.e. the subsets for a given scale have the shape of a tile, do not overlap, cover the whole image, the edge length is a power of two and the whole tile fits into the shared memory of one multiprocessor of a CUDA device. Despite its approximate nature, according to our tests presented in this paper, the ICD preserves the quality and statistical interpretation of the result obtained from the exact algorithm, but significantly improves the execution time. The speedups of the CUDA implementations are measured on simulated test data. The power of the new ICD is demonstrated by using it as preprocessor for the super-resolution optical fluctuation imaging (SOFI) method (Dertinger et al. 2009), a recent development in fluorescence microscopy. As the number of frames for SOFI applications has to be large enough to resolve the statistical properties of the fluorescence signal, for instance in case of quantum dots up to several thousand images are required, the performance of an SMRE is crucial for the feasibility of applying it as preprocessor.

This paper is organized as follows. Section 2 contains a basic description of the theory of multi-resolution and introduces the ADMM, Dykstra's algorithm, SOFI and the Fourier ring correlation (FRC) for the quantitative assessment of the resolution improvement. Section 3 highlights the key features of our implementation. For a complete listing see the accompanying source code. In Sec. 4 we discuss our results, which include tests of the performance and the resolution improvement of the two variants of Dykstra's algorithm. To study

the performance on real data obtained from an experiment we employ SMRE as pre- and postprocessor for SOFI. Finally, Sec. 5 gives a conclusion.

2 Statistical Multi-resolution Estimation

In statistical signal processing the noisy measurement $I \in \mathbb{R}^m$ of the signal $x \in \mathbb{R}^n$ is formulated as

$$I = A * x^* + \epsilon, \quad (1)$$

where A is the PSF of the imaging apparatus, x^* is the true signal underlying the measurement I and ϵ is a noise vector. The convolution of A and x^* is denoted as $A * x^*$. The estimates for the true signal and the noise, based upon knowledge of I , are written as \hat{x} and $\hat{\epsilon}$, respectively. In practice, both are unknown. The linear operator A is usually ill-posed which renders the inversion of Eq. (1) infeasible in any real world situation. In order to overcome this difficulty the problem is augmented with a regularization term $R(x)$. A common example for the regularization is total variation (TV)

$$R_{\text{TV}}(x) = \|x\|_{\text{TV}} := \sum_{i=1}^n \sum_{k=1}^d |((\nabla x)_i)_k|,$$

where d is 2 for planar images, and 3 for image stacks. The latter frequently occur in confocal microscopy. The outer sum over i is over all pixels and the inner sum computes the L_1 norm of the local intensity gradient. TV estimators perform well on natural images (Facciolo et al. 2009), which are expected to consist of smooth areas and sharp boundaries. The term R may be substituted with a more problem-specific term, see for example (Diekmann et al. 2001).

A multi-resolution estimator recovers the most regular vector

$$\hat{x} = \operatorname{argmin}_{x, \epsilon} G(\epsilon) + R(x) \text{ s.t. } I = A * x + \epsilon \quad (2)$$

with respect to $R(x)$, which fulfills the multi-resolution constraint

$$G(\epsilon) = \begin{cases} 0 & \text{if } \max_{s \in \Omega} c_s(\alpha) \sum_{i \in s} \epsilon_i^2 \leq 1 \\ \infty & \text{else} \end{cases}. \quad (3)$$

The function G is a reformulation of the constraint that the noise ϵ has to be normally distributed, $\epsilon \sim N(0, \sigma^2)$. Using an Anscombe transformation (Frick, Marnitz, and Munk 2013) the Poissonian noise of digital cameras can be transformed such that it approximately obeys a normal distribution. The image $I \in \mathbb{R}^m$ contains m pixels, which are indexed by the index set $\{1, \dots, m\}$. A multi-resolution analysis works on subsets $s \subset \{1, \dots, m\}$ of the pixel indexes. The set of all subsets of pixel indexes is denoted as

$$\Omega = \{s \mid s \subset \{1, \dots, m\}\}. \quad (4)$$

The feasible set generated by a subset s of pixel indexes is denoted as

$$\tau_s(x) := \{x \in \mathbb{R}^n \mid c_s(\alpha) \sum_{i \in s} x_i^2 \leq 1\}. \quad (5)$$

The intersection of all τ_s defines the feasible set

$$\tau_G := \bigcap_{s \in \Omega} \tau_s \quad (6)$$

of the multi-resolution constraint G .

In practical applications Ω will be restricted to connected areas of only a few pixels since the computational effort increases with $|\Omega|$, the cardinality of Ω . Then G computes the maximum squared residual on all subsets $s \in \Omega$. With an appropriate choice of the weights $c_s(\alpha)$ one can ensure that for each $e \in \{\epsilon \in \mathbb{R}^m \mid G(\epsilon) < \infty\}$ the noise $e|_s$ in the pixels belonging to a subset $s \in \Omega$ is Gaussian distributed with a chosen probability of at least α . Hence, the estimator \hat{x} is the smoothest image in the sense of R which satisfies the multi-resolution constraint enforced by G , as given in Eq. (3). This relation is visualized in Fig. 2.

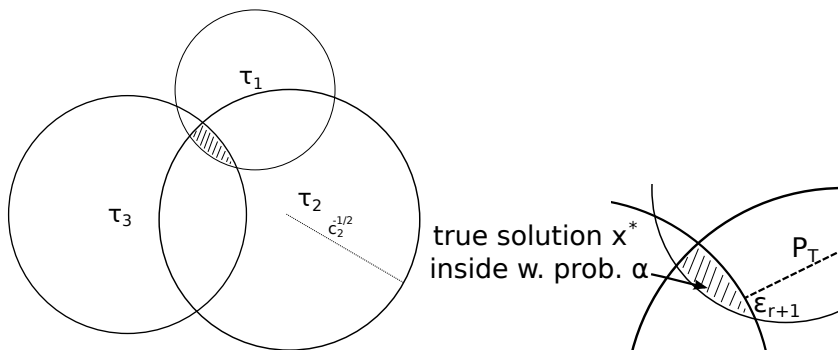


Figure 2: **Left:** The feasible sets are generated by the subsets $s \in \Omega$. Their dimensions are given by the cardinalities of the subsets s . The estimate \hat{x} is inside of the intersection of all spheres τ_s . **Right:** The unknown true solution x^* is inside of the feasible set with probability α .

2.1 Selection of the weights

The weights $c_s(\alpha)$ are required to ensure a balanced hypothesis test among all chosen subsets $s \in \Omega$ of the image plane. The probability that $\max_{s \in \Omega} c_s(\alpha) \sum_{i \in s} \epsilon_i^2 \leq 1$ is required to equal α for all sets. A method to choose $c_s(\alpha)$ accordingly is given in (Frick, Marnitz, and Munk 2013). The function

$$t_s(\epsilon) = \sum_{i \in s} \epsilon_i^2$$

measures the sum of squared residuals in a set s . Its fourth root transform

$$(t_s(\epsilon))^{1/4} \sim N\left(\mu_s = (|s| - 0.5)^{1/4}, \sigma_s^2 = \frac{1}{8\sqrt{|s|}}\right)$$

is approximately normally distributed. With this transformation each s contributes equally to the extreme value statistics

$$Q_\Omega = \max_{s \in \Omega} \frac{(t_s)^{1/4} - \mu_s}{\sigma_s}.$$

Then, an appropriate choice for the weights is

$$c_s(\alpha) = \frac{1}{(q_\alpha \sigma_s + \mu_s)^4}.$$

In this equation q_α is the α quantile of Q_Ω . It follows that

$$P\left(\max_{s \in \Omega} c_s(\alpha) t_s \leq 1\right) = \alpha,$$

i.e. the probability that Gaussian noise violates a single constraint is α . The probability to violate the constraint is balanced for all subsets by the choice of the $c_s(\alpha)$. Hence, the unknown true signal x^* itself fulfills the constraint with probability α ,

$$P(G(I - A * x^*) \leq 1) = \alpha. \quad (7)$$

Moreover, one can show (Frick, Marnitz, and Munk 2013) a sound statistical relation between the estimated signal \hat{x} and x^* with respect to the regularization R for the estimator in Eq. (2) applied to Eq. (1),

$$P(R(\hat{x}) \leq R(x^*)) \geq \alpha. \quad (8)$$

The probability that a feature in the recovered signal \hat{x} is in fact a feature of the true image x^* and not an artifact arising from incomplete noise removal is at least α .

2.2 Alternating Direction Method of Multipliers

The numerical minimization of Eq. (2) can be tackled by using the ADMM (Gabay and Mercier 1976; Hong and Luo 2012). The ADMM is a method to minimize a convex functional depending on a set of variables in the presence of constraints. The constraints are enforced by augmenting the functional with Lagrangian terms Υ , one for each constraint. The convergence speed is enhanced by adding a quadratic penalty term $\|I - (A * x + \epsilon)\|_2^2$, weighted by a real number $\rho > 0$ (Hong and Luo 2012). The constrained minimization problem in Eq. (2) then corresponds to the unconstrained minimization with respect to the primal variables $x \in \mathbb{R}^n$ and $\epsilon \in \mathbb{R}^m$, and maximization with respect to the dual variable $\Upsilon \in \mathbb{R}^m$ of the objective functional

$$\begin{aligned} \mathcal{L}(x, \epsilon) = & G(\epsilon) + R(x) + \frac{\rho}{2} \|I - (A * x + \epsilon)\|_2^2 \\ & + \langle \Upsilon, I - (A * x + \epsilon) \rangle. \end{aligned} \quad (9)$$

The solution $\hat{x} = \operatorname{argmin}_{x, \epsilon} \max_{\Upsilon} \mathcal{L}(x, \epsilon)$ is obtained iteratively, cf. Algorithm 1. The estimate after r iterations of the ADMM is denoted as x_r . In the limit $r \rightarrow \infty$ it converges towards the minimum, $x_r \rightarrow \hat{x}$. The minimization with respect to x can be evaluated in linear approximation, without damaging the overall convergence (Hong and Luo 2012). The update rule for Υ as given in Algorithm 1 corresponds to the method of steepest ascent. To simplify the minimization we decouple the deconvolution and smoothing by introducing another variable z . Hence the problem

$$\hat{x} = \operatorname{argmin}_{x, \epsilon} G(\epsilon) + R(z) \text{ s.t. } I = A * x + \epsilon, \quad z = x, \quad (10)$$

Algorithm 1 Alternating Direction Method of Multipliers

choose $\delta > 0$, $x_0 \in \mathbb{R}^n$, $\Upsilon_0, \epsilon_0 \in \mathbb{R}^m$, $\rho > 0$
while $\|x_r - x_{r-1}\|_2 > \delta$ and $\|I - (A * x_r + \epsilon_r)\|_2 > \delta$ **do**
 $x_{r+1} = \operatorname{argmin}_x \mathcal{L}(x, \epsilon_r)$
 $\epsilon_{r+1} = \operatorname{argmin}_\epsilon \mathcal{L}(x_{r+1}, \epsilon)$
 $\Upsilon_{r+1} = \Upsilon_r + \alpha (I - (A * x + \epsilon))$
end while

has two constraints. This leads to the augmenting variables Υ_1 , Υ_2 , ρ_1 , and ρ_2 . The result \hat{x} is not altered by this additional constraint, but the individual steps in the ADMM become easier to solve. The introduction of z does not perturb the convergence of the ADMM in linear approximation of $\mathcal{L}(x, \epsilon_r)$. To further reduce the error in each iteration step a stabilization term $\gamma \|x\|_2^2$ is introduced, which leads to a modified update rule

$$x_{r+1} = \operatorname{argmin}_x \frac{\rho_1}{2} \|I - A * x - \epsilon\|_2^2 + \langle \Upsilon_1, I - A * x - \epsilon \rangle + \frac{\rho_2}{2} \|x - z\|_2^2 + \langle \Upsilon_2, x - z \rangle$$

which can be used in its linearized version

$$x_{r+1} \approx \operatorname{argmin}_x \gamma \|x\|_2 + \langle \Upsilon_2 - A^T * (\rho_1 (I - \epsilon) + \Upsilon_1) - \rho_2 z, x \rangle. \quad (11)$$

Here, A^T denotes the transpose of the matrix A . The minimization with respect to x has no closed form since A is ill-posed. As long as γ is chosen sufficiently large, x_r still converges to \hat{x} for large r . The minimization with respect to ϵ can be rewritten as a projection on the intersection of convex sets,

$$\epsilon_{r+1} = P_G \left(I - A * x + \frac{\Upsilon}{\rho} \right), \quad (12)$$

where, $P_G(\cdot)$ is defined as

$$P_G(X) := \operatorname{argmin}_\epsilon \left\{ G(\epsilon) + \frac{\rho}{2} \|\epsilon - X\|_2^2 \right\}. \quad (13)$$

2.3 Dykstra's Algorithm

The problem of projecting on the feasible set τ_G of the multi-resolution constraint G is solved using Dykstra's algorithm (Dykstra 1983; Gaffke and Mathar 1989), which requires the knowledge of the projections p_s on each of the sets $\tau_s(\epsilon)$. In general, the projection on a set $\tau_s(x)$ is defined as

$$p_s(x_{i \in s}) = \begin{cases} \frac{x_i}{\sqrt{c_s(\alpha) \sum_{i \in s} x_i^2}} & \text{if } c_s(\alpha) \sum_{i \in s} x_i^2 > 1 \\ x_i & \text{else} \end{cases}, \quad (14)$$

where $\|x\|_{2,s}^2 := \sum_{i \in s} x_i^2$ is the L_2 norm with respect to the pixels belonging to the set $s \in \Omega$. This projection is to be performed in each iteration of the ADMM. Therefore, its performance is critical for the overall minimization. The projection on τ_G is computed iteratively as shown in Algorithm 2. The algorithm

Algorithm 2 Dykstra's Algorithm

choose $\delta > 0$, given $x_0, q_0 \in \mathbb{R}^n$ with $q_{0,s} = 0 \quad \forall s \in \Omega$
while $\|x_r - x_{r-1}\|_2^2 > \delta$ **do**
 $x_{r+1} = p_s(x_r - q_{r,s})$
 $q_{r+1,s} = x_{r+1} - x_r$
end while

is known to converge towards the projection of x_0 on the intersection of the $s \in \Omega$. The iteration is stopped when the change in x_r is below some chosen threshold δ . In the context of image processing the sets s denote small subsets in the image. The projection on two sets $s_1, s_2 \in \Omega$ can be calculated in parallel if $s_1 \cap s_2 = \emptyset$. However, the order in which the projections are performed is crucial for the convergence of the algorithm. Therefore, only non-overlapping subsequent projections can be calculated in parallel.

2.4 SOFI

Recently, several methods have been developed to overcome the diffraction limit (first derived by Abbe) on resolution in optical microscopy, such as PALM (photo-activation localization microscopy) (Hess, Girirajan, and Mason 2006), STORM (stochastic optical reconstruction microscopy (STORM) (Rust, Bates, and Zhuang 2006) SIM (structured illumination microscopy) and its nonlinear variant (Gustafsson 2005) and most notably the STED (stimulated emission depletion) (Hell and Wichmann 1994) microscopy which was awarded the Nobel prize in Chemistry, 2014. All of these methods require to some extent special sample preparation techniques making these methods more elaborate and complicated than traditional fluorescence wide-field microscopy.

A different approach is SOFI (super-resolution optical fluctuation imaging) (Dertinger et al. 2009; Dertinger et al. 2010) which infers the additional information necessary for resolution improvement from the temporal behavior of the signal of the imaged object which in case of fluorescence microscopy works as follows. Given N point-like emitters, the fluorescence signal at an arbitrary point $\mathbf{r} \in \mathbb{R}^3$ (in practice this is a pixel) in the image plane can be written as

$$F(\mathbf{r}, t) = \sum_k U(\mathbf{r} - \mathbf{r}_k) \varepsilon_k s_k(t), \quad (15)$$

where $U : \mathbb{R}^d \rightarrow \mathbb{R}^d$ is the PSF, which is entirely determined by the optical system and time-independent. In the following we restrict the discussion to the focus and image plane, i.e. $d = 2$. The molecular brightness of the k th fluorophore is denoted as $\varepsilon_k \in \mathbb{R}^+$ and the stochastic time-dependence of its emitted fluorescence is $s_k(t) : \mathbb{R} \rightarrow [0, 1]$. With $\langle \dots \rangle_t$ as average over time, the fluctuations $\delta F(\mathbf{r}, t) = F(\mathbf{r}, t) - \langle F(\mathbf{r}, t) \rangle_t$ of the observed fluorescence are given by

$$\delta F(\mathbf{r}, t) = \sum_k U(\mathbf{r} - \mathbf{r}_k) \varepsilon_k \delta s_k(t). \quad (16)$$

To motivate the idea underlying the SOFI signal we consider the two-point

correlation function $G_2(\mathbf{r}, \tau) = \langle \delta F(\mathbf{r}, t + \tau) \cdot \delta F(\mathbf{r}, t) \rangle_t$ which by Eq. (15) is

$$G_2(\mathbf{r}, \tau) = \sum_k U^2(\mathbf{r} - \mathbf{r}_k) \varepsilon_k^2 \langle \delta s_k(t + \tau) \cdot \delta s_k(t) \rangle_t. \quad (17)$$

To get a value equivalent to the intensity the final SOFI signal is given by the integrated correlation

$$I_{SOFI}(\mathbf{r}) = \sum_k U^2(\mathbf{r} - \mathbf{r}_k) \varepsilon_k^2 \int_{-\infty}^{+\infty} \langle \delta s_k(t + \tau) \cdot \delta s_k(t) \rangle_t d\tau. \quad (18)$$

In general, instead of correlation functions cumulants C_n are used, where n denotes the order. The advantage of cumulants is the absence of correlations of orders less than n . Then, the intensity $I_{SOFI}(\mathbf{r})$ assigned to a pixel in the final SOFI image is proportional to the n th power of the PSF. Usually, a Gaussian profile is a good approximation to the shape of the PSF and thus resolution is improved by a factor of \sqrt{n} if a cumulant of order n is used. However, at the same time inhomogeneities in the molecular brightnesses ε_k are amplified as well, as already the simple case of order 2 in Eq. (18) shows.

A common simplification, especially for higher order SOFI methods, is to approximate the integral by the maximal value of the integrand, which for order 2 is simply the variance of the intensity in a pixel

$$C_2(\mathbf{r}, 0) = \langle F^2(\mathbf{r}, t) \rangle_t - \langle F(\mathbf{r}, t) \rangle_t^2. \quad (19)$$

For higher orders the cumulants can be computed from the moments of the probability distribution of the fluctuations.

The strength of SOFI is that it can be combined with a variety of microscopy techniques without any need for modifying the experimental setup as it is a software-only, pure post-processing method. Its disadvantage is that it needs a sufficient amount of images to resolve the statistical behavior of the temporal fluctuations of the observed (usually fluorescence) signal. However, STORM has the same drawback.

2.5 Fourier ring correlation

In order to assess the quality of an estimator on experimental data an estimate for image resolution is necessary. The Fourier ring correlation (FRC) quantifies the image resolution from correlations in Fourier space and the impact of noise on those correlations. It was specifically designed for the case where the true signal is not known. Originally, the FRC was conceived as resolution measure for electron microscopy images (Saxton and Baumeister 1982). Recently, it was proposed as resolution criterion for optical super-resolution microscopy (Nieuwenhuizen et al. 2013; Banterle et al. 2013).

To compute an FRC the correlation along circles in the Fourier plane is calculated for different realizations of the noise. The FRC defines image resolution as the smallest distance at which the correlation of two considered realisations of the same statistical process drops below the predicted correlation for pure noise. Given two realizations $I_1, I_2 \in \mathbb{R}^n$ of the same noisy image acquisition

process, the correlation of the Fourier transformed images \tilde{I}_1, \tilde{I}_2 , constrained to a ring in distance r to the origin, is calculated as

$$FRC(r) = \frac{\sum_{r_i \in r} \tilde{I}_1(r_i) \cdot \tilde{I}_2^*(r_i)}{\sqrt{\left(\sum_{r_i \in r} |\tilde{I}_1(r_i)|^2\right) \cdot \left(\sum_{r_i \in r} |\tilde{I}_2(r_i)|^2\right)}}. \quad (20)$$

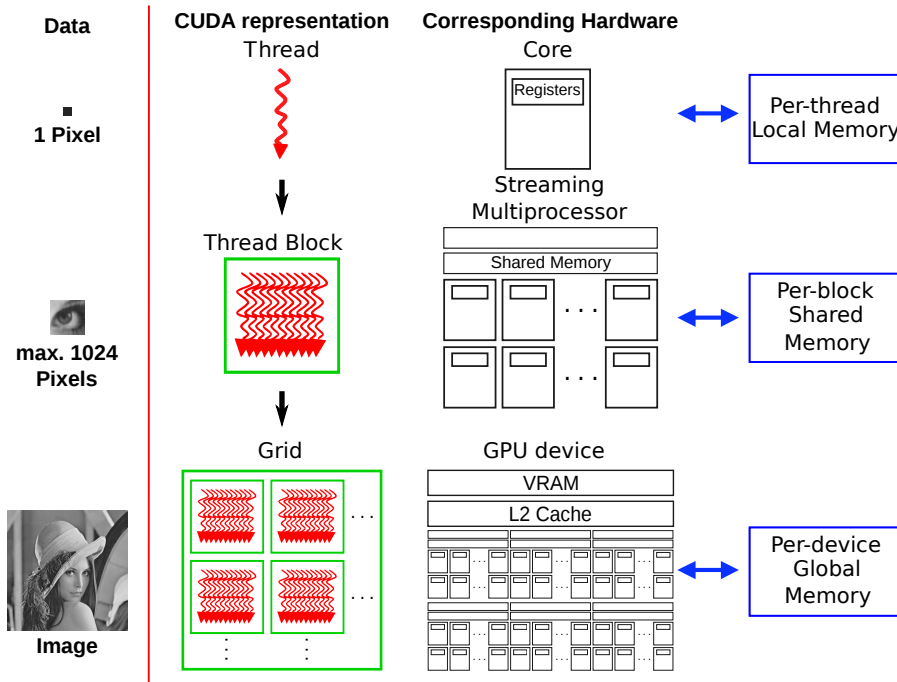


Figure 3: The block diagram illustrates the mapping of parallel processing of data (left) to the programming structure of CUDA (middle). This structure is mainly modeled following the hardware design of GPUs (right), especially the memory hierarchy.

3 Implementation

The core of an implementation of an SMRE is the ADMM algorithm for minimizing Eq. (10). The operator A is approximated as Gaussian kernel with the standard deviation σ_{PSF} given as input parameter, cf. the parameter listing in the appendix. The implementation is based on the SciPAL library.

The numerically expensive part is the implementation of Dykstra’s algorithm, cf. Algorithm 2. We first discuss the implementation which strictly follows the mathematical description as given in Sec. 2.3, which we call the *exact method* (Sec. 3.1). Then we discuss our *incomplete method* (Sec. 3.2), which, according to our numerical experiments, is equivalent to the exact method, but much simpler to implement because it partitions the image in non-overlapping sets right from the beginning. For both variants the runtime mainly depends on the maximum

size of the subsets and the size of the image. In general, subsets and images may have virtually any shape. Therefore, we introduce an effective edge length L_s for the subsets and L_I for images. Both are defined as the square root of the number of pixels in a subset and an image, respectively. We further define the maximum multi-resolution depth

$$K_{\text{SMRE}} := \log_2 \left(\max_s L_s \right) \quad (21)$$

and the associated maximum resolution scale

$$L_{\text{SMRE}} := 2^{K_{\text{SMRE}}}. \quad (22)$$

For readers not familiar with the CUDA programming model we provide a brief description in Appendix A. A graphical summary of our way mapping data to the GPU is given in Fig. 3.

3.1 Dykstra’s Algorithm (exact Version)

The parallelized implementation of Dykstras’s algorithm is the key to reach high speedups. Figure 4 shows simplified block diagrams of the serial implementation (a), of the ICD (b) and of the exact method (c). Only non-overlapping subsequent projections p_s can be calculated in parallel and the sequence of overlapping subsets needs to be preserved. This constraint is the principal guiding line for the implementation.

Each group is limited to a maximum size of 1024 pixels per group if each thread works on one pixel as this is the maximum number of threads per thread block. If the next set to be added to a group during creation exceeds this limit a new group is formed, leaving some threads idle in the former group. Therefore, in general not all threads of a thread block are in use. To avoid blocking behavior within a group, the subsets of pixels must be chosen such that only projections on mutually non-overlapping sets occur. The groups of subsets are stored in a linked list, in the following called execution queue, which defines the sequence in which they are processed. The order in which projections are carried out has to be such that the distance between overlapping subsets is large. In this context, distance is meant with respect to the positions in the execution queue.

The efficient computation on GPUs faces two further problems. (i) The limited amount of VRAM is not sufficient to store all necessary data on the GPU. The memory needed to store all q_s variables crucially depends on the multi-resolution scale L_{SMRE} and the number of pixels in an image L_I^2 , and is $\mathcal{O}(L_{\text{SMRE}}^3 L_I^2)$. For instance, for a 1024×1024 pixel image and $L_{\text{SMRE}} = 15$ this amounts to 14 GB for single-precision. (ii) To populate all the SMs in order to achieve good efficiency when calculating the parallel projections. The classical approach of starting a single CUDA kernel is not efficient due to the blocking behavior of overlapping subsequent projections and the insufficient amount of memory on the GPU. We have to use the conventional RAM on the CPU side as additional buffer for temporary data which requires frequent memory transfers before and after the execution. Instead, we make use of CUDA’s Hyper-Q feature to implement a multi-stream based parallelization.

A key element of our implementation is a pool of worker threads on the host side, where each one uses a CUDA stream to process items received from a

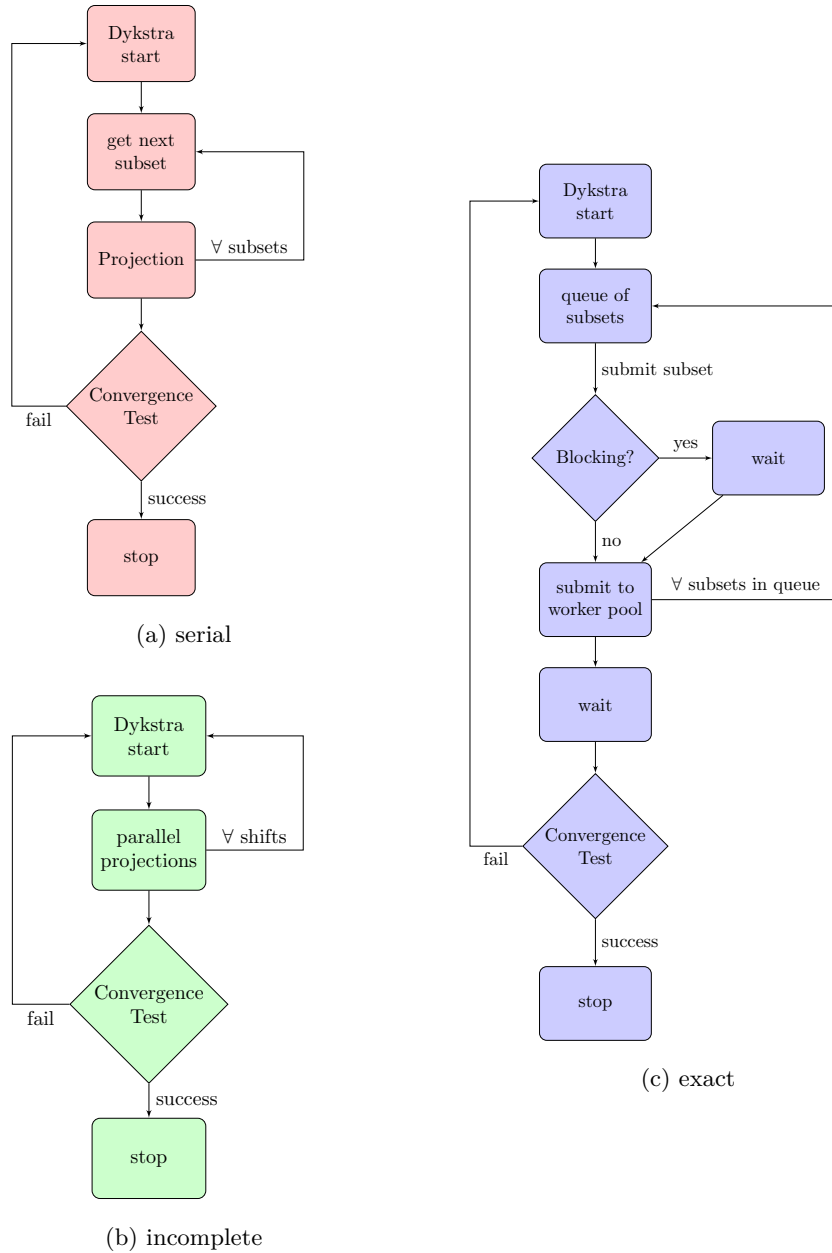


Figure 4: Differences between a serial implementation (a) and the presented parallel exact (c) and incomplete (b) implementations. Only non-overlapping subsequent projections can be calculated in parallel and the sequence of overlapping subsets needs to be preserved. This constraint shaped the implementation of the exact method, as it has to check for overlapping (blocking) subsets. The performance of the exact method is mainly limited by the transfer rate of the PCIe bus due to the limited RAM on the GPU. See Fig. 5 for a detailed discussion on the CUDA kernels of the parallel projection methods. The incomplete method works on a set of subsets which is tailored for concurrent execution. This increases the performance. The serial approach performs the projections one after another.

shared queue. The queue holds the groups of subsets. Before adding the groups to the queue, the main worker thread verifies that the group to be added does not overlap with groups already queued. If an overlap is detected, the thread waits until the blocking group is processed and removed from the queue. Only the main thread which adds groups of subsets to the queue is subject to long blocking behavior. The GPU always has a high work load as memory transfers and instruction execution are done concurrently on multiple streams. Listing 1 shows the stream handling in the worker thread which coordinates the work on a CUDA stream. It retrieves several groups of subsets at once from the queue, and then adds copy and execution instructions to a CUDA stream to process a list of groups (a cluster) in parallel. For brevity, uninteresting parts of the source code like error checking have been omitted from the listing. Groups are designed to be processed by a thread block. This implementation launches the kernel in a grid of many thread blocks. The memory transfers are sufficiently large to make the use of multiple streams an effective latency hiding mechanism.

Listing 1: The parallel worker threads which control the CUDA streams

```

1 // This function is executed by 'stream_count' threads in
2 // parallel, each creates an CUDA stream and coordinates
3 // the work done on that stream. It removes items from
4 // the queue and processes them. End thread when terminate
5 // item is recieved from the queue.

7 // 'group' is a class which contains a group of subsets
8 // 'T' can be float or double
9 template<typename group, typename T>
10 void stream_handler() {
11     // CUDA device id has to be set by each thread
12     cudaSetDevice(inf->device_id);

13
14     // Create CUDA stream
15     cudaStream_t mystream;
16     cudaStreamCreate(&mystream);

17
18     // Remove several groups from queue on each get() call
19     std::list<group*> cluster_vec;
20     // Maximum number of groups we try to get from queue
21     const int max_num_cluster = 128;
22     // Minimum number of groups we try to get from queue, not
23     // guaranteed
24     const int min_num_cluster = 12;

25     // Allocate the maximum needed memory on host and device for
26     // cluster information and q_offset

27
28     // Array of device pointers which contains the information
29     // about the clusters

30     SciPAL::Vector<*int, blas> cluster_info(4*max_num_cluster);
31     SciPAL::Vector<*int, cublas> cluster_info_d(4*max_num_cluster);

32
33     // Where to find the q values for each thread block
34     SciPAL::Vector<int, blas> q_offset(max_num_cluster);
35     SciPAL::Vector<int, cublas> q_offset_d(max_num_cluster);

36
37     // All q values
38     SciPAL::Vector<T, cublas> q_d(1024*max_num_cluster);
39

```

```

41     step35::Kernels<T> kernels;
42
43     // Get a list of min_num_cluster to max_num_cluster clusters
44     cluster_vec = queue->get(min_num_cluster, max_num_cluster);
45
46     // Big while loop until terminate signal is received
47     while ( cluster_vec.front()->size != 0 ) {
48         // Number of groups we received from queue
49         int num_of_cluster = cluster_vec.size();
50
51         // Fill arrays q_offset and cluster_info with the
52         // device pointers to the desired information
53         // ...
54
55         // In the big q array, where can I find the q for
56         // the first pixel of my cluster?
57         unsigned int offset = 0;
58
59         // Copy q for all frames to device
60         for (auto it=cluster_vec.begin(),
61              end=cluster_vec.end(); it!=end; ++it) {
62             cudaMemcpyAsync(&(q_d[offset]), (*it)->qmat,
63                             (*it)->size*sizeof(T),
64                             cudaMemcpyHostToDevice, mystream);
65             offset+=(*it)->size;
66         }
67
68         // Add copy command of cluster_info and q_offset
69         // from host to device to CUDA stream
70         // ...
71
72         // Start a Dykstra's CUDA kernel on all frames in
73         // the list of clusters we received
74         kernels.dykstra(q_d, inf->e_d, cluster_info_d, q_offset_d,
75                         num_of_cluster, inf->width, inf->height,
76                         1024, &mystream);
77
78         // Add copy command of q from device to host to
79         // our CUDA stream
80         // ...
81
82         // Block until our CUDA stream has completed all operations
83         cudaStreamSynchronize(mystream);
84
85         // Signal queue that task is done
86         queue->task_done(cluster_vec);
87
88         // Get a list of min_num_cluster to max_num_cluster
89         // groups from queue
90         cluster_vec = queue->get(min_num_cluster, max_num_cluster);
91     } // End big while loop
92
93     // Worker thread shutdown cleanup
94     // ...
95 }

```

3.2 Incomplete Projection

The exact variant has some limitations which hinder an efficient CUDA implementation, such as the PCIe bottleneck and the overall complexity of the

detection of overlapping sets. To further adapt Dykstra’s algorithm to the execution on a CUDA device we now restrict the eligible subsets of the image plane to only those which are formed by squares with edge lengths of powers of 2, up to $L_{\text{SMRE}} = 32$. Fig. 4 shows a general overview of the discussed implementations, Fig. 5 shows the difference in the chosen subsets between the exact and incomplete implementation.

All shifts which are a power of 2 up to 32 of these squares are considered. Consider the set of non-overlapping squares in the image plane with edge lengths 2^k , with $k \leq K_{\text{SMRE}} := 5$. If the origin of each square is shifted by 2^k in each direction the pattern is mapped onto itself. Only shifts by 2^i pixels in each direction with $i < k$ pose a mapping on a different pattern. The set $\tilde{\Omega}_k^i$ denotes all non-overlapping squares with an edge length 2^k which are shifted by 2^i pixels. Then construct the sets

$$\Omega^i = \bigcap_{i \leq k \leq 5} \tilde{\Omega}_k^i.$$

The incomplete projection

$$P_{\text{incomplete}}(x) = \prod_{i=0}^5 P_{\Omega^i} x$$

is computed as the projection on each Ω^i subsequently. The resulting residual is still in the allowed set of G in Eq. (9), which preserves the statistical interpretation of the result.

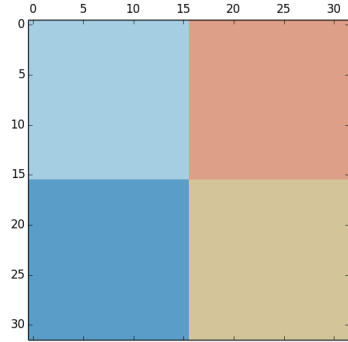
The projection on a set Ω^i is calculated in a single CUDA kernel (Listing 3). The kernel takes as input a pointer e to the residual vector on the device, the dimension of the vector (ni , nj) and the offset (offset_i , offset_j) from where to generate the subsets. The shifting is carried out as shown in Listing 2 by calling the kernel with different offsets i . This increases the number of considered subsets. The edge length 2^{smmin} of the smallest subsets can be specified to avoid unnecessary duplicate computations as a result of the shifting. As in the kernel for the exact projection we make use of shared memory for the temporary arrays q , s_1 , s_2 . The exact projection kernel uses 12 bytes of shared memory in case of single-precision and 24 bytes for double-precision per thread, the incomplete kernel uses 32 bytes for single-precision per thread. The shared memory is limited to 48KB per thread-block. For a reasonable implementation of the ICD we need the full 1024 threads per thread block rendering computations in double-precision infeasible on all existing generations of the CUDA architecture.

Listing 2: Wrapper function around the incomplete Dykstra kernel

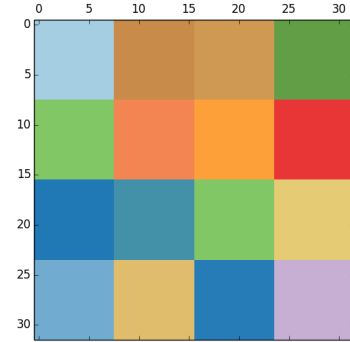
```

1  template<typename T>
2  void ICD_handler() {
3      int gridsi = info->width/32;
4      int gridsj = info->height/32;
5      dim3 grid(gridsi,gridsj);
6      dim3 blocks(1024,1);
7      for (int i = 0; i < 5; i++) {
8          __incomplete_dykstra<T><<<grid,blocks>>>(info->e_device,
9                                                    info->width,
10                                                 info->height,
11                                                 2^i, 2^i, i);
12     }
13 }

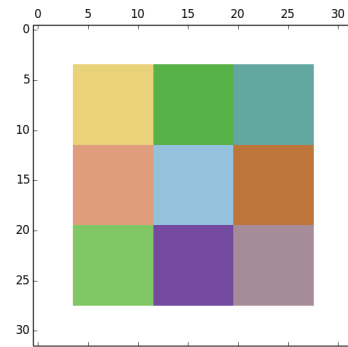
```

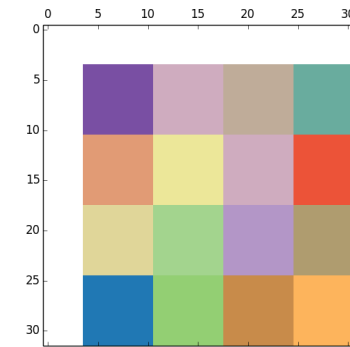
(a) Thread block pattern used in both incomplete and exact method



(b) Thread block pattern used in both incomplete and exact method



(c) Thread block pattern used only in exact method



(d) Thread block pattern used only in exact method

Figure 5: Visualization of the differences between the exact and the incomplete method. The illustrations show 32×32 pixel sections of the larger image, each section is processed by one CUDA thread block of 1024 threads. The incomplete method makes optimal use of thread blocks by using subsets of Ω of edge length 1, 2, 4, 8, 16 and 32 pixels which fill up a 32×32 pixel section. The subfigures (a) and (b) show the pattern of subsets of edge length 16 and 4 pixels respectively. While the exact method uses all subset patterns of the incomplete method it also includes subsets of Ω with all edge lengths and all possible shifts within the image. The patterns (c) and (d) are thus only used in the exact method and not in the incomplete method.

Listing 3: incomplete implementation of Dykstra's algorithm

```

1 // CUDA adapted incomplete Dykstra projection
2 // @param e pointer to the residual
3 // @param ni height of the image
4 // @param nj width of the image
5 // @param offseti offset in vertical direction
6 // @param offsetj offset in horizontal direction
7 // @param smin minimum subset size is  $2^{smin}$ 
8
9 // 'T' can be float or double, on current hardware only float is
10 // supported
11 template<typename T>
12 __global__ void
13 __incomplete_dykstra(T *e, const int ni, const int nj, const int
14   offseti, const int offsetj, const int smin) {
15   // Allocate temporary arrays q, s1, s2 in shared memory
16   // ...
17
18   // Set q = 0
19   for (int s=5; s>=0; s--) {
20     q[s*1024+threadIdx.x]=0;
21   }
22
23   // Temporary variables
24   unsigned int is, js, idx;
25
26   // Tolerance
27   const T tol = TOLERANCE; //= 1e-3
28
29   // Do parallel projections until convergence test passes
30   T delta = 2.0*tol;
31   while ( delta > tol*1024.0 ) {
32     delta = 0;
33     // Wait for all threads before starting the iteration
34     __syncthreads();
35
36     // In one threadblock we apply dykstra's algorithm to
37     // subsets with edge lengths 32, 16, 8, 4, 2 and 1.
38     // Each thread processes one pixel.
39     for (int s = 5; s >= smin; s--) {
40       // Edge length of the subset =  $2^s$ 
41       int SubsetLength = pow_of_two(s);
42       // Number of subsets in one threadblock =  $2^{5-s}$ 
43       int SubsetNum = pow_of_two(5 - s);
44       // Number of pixels in each subset =  $2^{2*s}$ 
45       int SubsetSize = pow_of_two(2*s);
46       // Get Line in global image, assign to is
47       // ...
48       // Column in global image, assign to js
49       // ...
50       // For this iteration this thread is supposed
51       // to process the pixel (is, js), the pixel
52       // index idx in the global image is given by:
53       idx = is*nj + js;
54
55       // Fill shared memory with variables we use later
56       s1[threadIdx.x] = e[idx] - q[s*1024+threadIdx.x];
57       s2[threadIdx.x] = s1[threadIdx.x]*s2[threadIdx.x];
58       // Wait for all threads
59       __syncthreads();
60
61       // Index to first pixel of my subset

```

```

        int SubsetStartIdx = (threadIdx.x/SubsetSize)*
SubsetSize;
61
        // Sum over all pixels of one subset, write the result
63 // to s2[SubsetStartIdx]
        while (m <= pow_of_two(2*s-1)) {
65             if (threadIdx.x - SubsetStartIdx + m < SubsetSize)
{
                s2[threadIdx.x] += s2[threadIdx.x + m];
67             }
            m = m << 1; // m = m*2
69             __syncthreads();
        }
71
        //  $q = x_{r+1} - x_r$ 
73 q[s*1024 + threadIdx.x] = -s1[threadIdx.x];
75
        // Eq. (14) from Dykstra's algorithm
        // 'cs' is a array allocated in CUDA constant memory
77 if (cs[s]*s2[SubsetStartIdx] > 1.0) {
            s1[threadIdx.x] /= sqrt(cs[s]*s2[SubsetStartIdx]);
79         }
        // Update q
81 q[s*1024+threadIdx.x] += s1[threadIdx.x];
        // Calculate increment, mabs is our abs function
83 delta+=mabs(e[idx] - s1[threadIdx.x]);
85
        // Update the estimate of residual
        e[idx] = s1[threadIdx.x];
87 // Wait for all threads before next step
        __syncthreads();
89     }
}
91 }

```

4 Results

The CUDA implementation of the new ICD variant is found to be 100 times faster than a serial implementation of Dykstra’s algorithm and 10 times faster than the CUDA implementation of the exact version. Yet, it reconstructs images nearly as well as the exact implementation, i.e. for the naked eye the results are indistinguishable. Both implementations proved robust against noise and blur. The runtime performance is tested on synthetic images of different sizes. Because of the enormous memory consumption of the exact variant of Dykstra’s algorithm we had to vary the SMRE depth K_{SMRE} for the different tests in order to keep the computations feasible. As an example of a real-life application we use the ICD as pre- and postprocessor for the SOFI algorithm which gives a further increase in resolution of up to 30%.

4.1 Test Data

To assess the quality of the estimator we use synthetic data generated from the standard Lena image with simulated noise and blur. For synthetic data the true signal is known and the quality of the reconstruction algorithm can be estimated directly. Figure 6a shows the unperturbed standard Lena test image. The simulated test image (Fig. 6b) is generated by blurring the original image with a Gaussian kernel of width $\sigma_{\text{PSF}} = 4 \text{ px}$ (px = pixel) and adding Gaussian noise with a standard deviation of $\sigma = 1$. The noise strength $\sigma = 1$ corresponds to about 0.5% of the maximum signal and is given in gray levels. We generated further test images with smaller signal to noise ratios, $\sigma = 3$ and $\sigma = 10$ (not shown), for comparison.

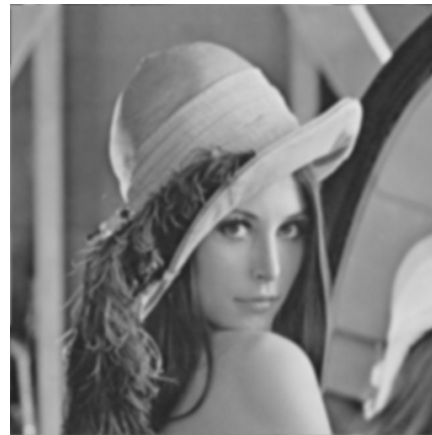
To assess the performance in real applications we study the combination of SMRE with SOFI (see Sec. 2.4) on experimental data.

The final test of the exact and incomplete implementation of Dykstra’s algorithm is done on optical widefield microscopy data, previously analyzed with the SOFI framework (Huss et al. 2013) in order to study the details of intracellular trafficking and assembly of GABA-B neurotransmitter receptors in hippocampal neurons. The data set represents a time series of the temporal fluctuations of the fluorescence signal of a nerve cell labeled with quantum dots which attach to the receptors. The fluctuations of the fluorescence stems from the blinking behavior of the quantum dots which is random and follows a power-law for the on- and off-times (Kuno et al. 2001). The movie consists of 3091 frames. Besides the considerable amount of out-of-focus light due to the widefield illumination, each image shows the noise and blur typical for optical imaging. A sample frame from the raw data is shown in Fig. 7a. The blur occurs due to the diffraction limit. The microscope records the real object convolved with the PSF. We approximate the convolution kernel as Gaussian. In terms of the SMRE framework this is the measurement operator.

The images are typically acquired in the photon-limited regime. Hence one has to deal with Poissonian noise disturbing the image, i.e. to apply the Anscombe transformation before running the SMRE.



(a) Test image, true signal.



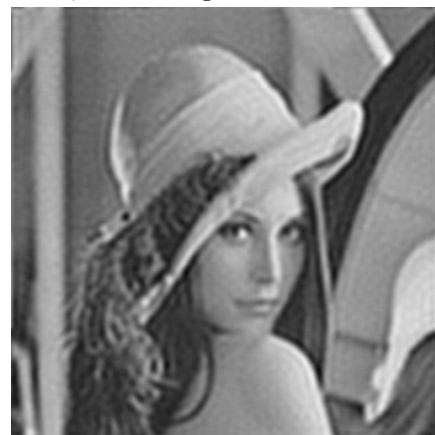
(b) Test image with simulated blur and Gaussian noise of strength $\sigma = 1$.



(c) Reconstruction using exact implementation, noise strength $\sigma = 1$.



(d) Reconstruction using incomplete implementation, noise strength $\sigma = 1$.



(e) Reconstruction using incomplete implementation, noise strength $\sigma = 3$.



(f) Reconstruction using incomplete implementation, noise strength $\sigma = 10$.

Figure 6: Test of the algorithms on the Lena image, for details refer to Secs. 4.1 and 4.3.

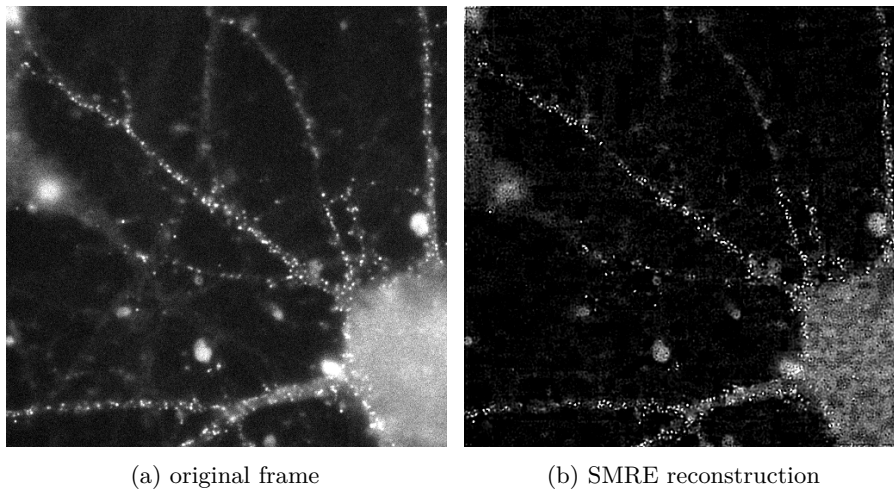


Figure 7: Sample frame from the experimental time series of the hippocampal neurons (Huss et al. 2013) (a), and its SMRE reconstruction (b).

4.2 Performance

Figure 8a compares the runtime of 100 ADMM iterations (in each iteration step Dykstra’s projection algorithm is run until convergence) between a serial implementation on a CPU (Intel Xeon X5675) and the exact and incomplete implementation on a NVIDIA Tesla K20c GPU. For all variants we used a fixed tolerance of 10^{-3} for the Dykstra algorithm. For the exact GPU and the serial CPU implementation the runtime depends on the number of subsets. The number of subsets for the incomplete GPU implementation only depends on the edge length of the image L_I . The plots do not include the startup time required for the initialization of the algorithms. While the main factor of the startup time for the incomplete implementation is the time needed to load the image, the startup time for the exact and CPU variants depends on the number of subsets. The latter algorithms need to preallocate memory for each q_s array of every subset s . For the plots the maximum multi-resolution scale is $L_{\text{SMRE}} = 15$ to make the computations feasible. As explained in Sec. 3.1 the exact method then requires 14 GB of memory when run in single precision. The runtimes of the different methods are considerably different. The incomplete method achieves an overall speedup of up to 100 over the single-threaded CPU implementation and is 10 times faster than the exact method.

4.3 Estimator quality

Based on the standard Lena test image, cf. Sec. 4.1, we analyze the quality of the statistical multi-resolution estimator. Figure 6 summarizes the results from both implementations for $\sigma = 1$ (Figs. 6c and 6d) and the ICD results for $\sigma = 3$ (Fig. 6e) and $\sigma = 10$ (Fig. 6f). All reconstructions use a maximum multi-resolution scale of $L_{\text{SMRE}} = 32$. The reconstructed image obtained from the exact implementation of Dykstra’s algorithm (Fig. 6c) is visually almost indistinguishable from the result obtained from the ICD variant (Fig. 6d), which

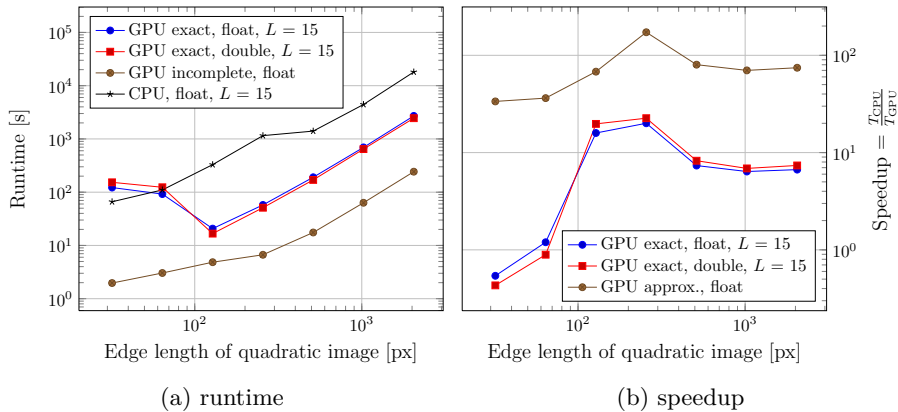


Figure 8: Runtime (a) and speedup (b) for 100 ADMM iterations. The exact GPU variants and the CPU variants use a maximum multi-resolution scale $L_{\text{SMRE}} = 15$. All runtimes given exclude the startup time.

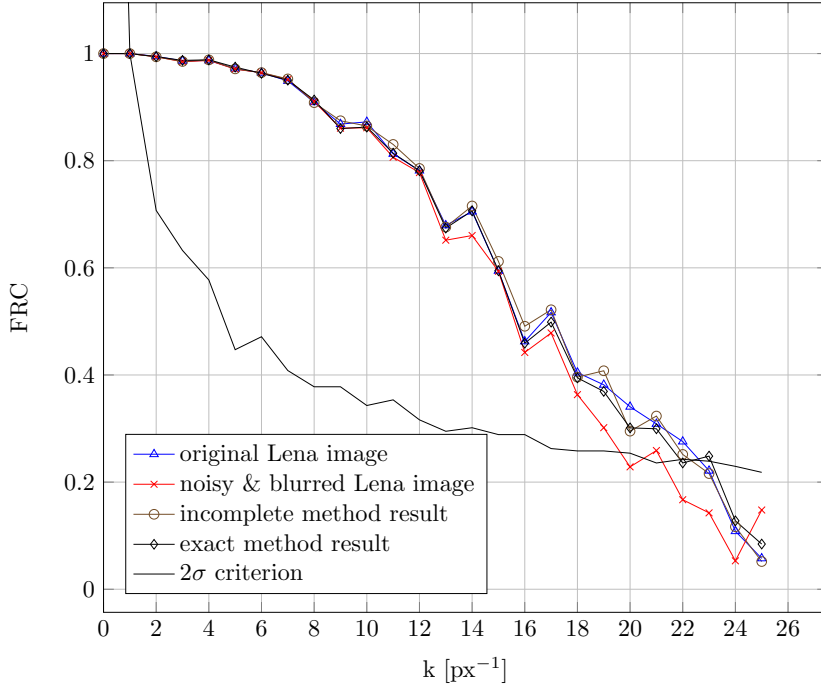
is quantitatively confirmed by the FRC, cf. Fig. 9a.

The FRC as described in Sec. 2.5 provides a quantitative measure of the resolution. Figure 9a shows the FRC of the Lena images displayed in Fig. 6. Visual inspection and the FRC indicate that the SMRE methods improve the image resolution and that the results of the exact and incomplete implementation are nearly identical.

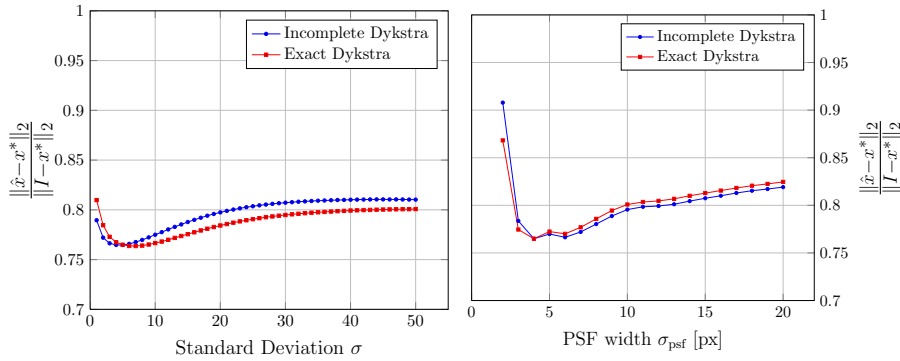
An important aspect of an estimator is robustness against noise strength and PSF radius. Typically estimators tend to decrease in quality with increasing noise strength and PSF radius. This behavior is investigated numerically in Fig. 9b and Fig. 9c, where the robustness against noise and PSF radius is plotted as L_2 -error $\|\hat{x} - x^*\|_2$ of the reconstruction \hat{x} with respect to the true signal x^* , normalized by the error $\|I - x^*\|_2$ of the simulated/measured image I . Values below 1 indicate an improvement in quality of the reconstruction over the measurement. Instabilities in the estimator become visible by observing the proposed ratio. Figure 9b shows the robustness against noise strength for fixed PSF radius $\sigma_{\text{PSF}} = 4$ px. The estimators are robust even for large noise. For small noise is the incomplete estimator slightly less efficient. The plot indicates that the quality of the exact estimator is better in terms of the L_2 -distance to the true signal compared to the incomplete estimator. The L_2 -distance plot for the robustness against the PSF radius with a fixed noise level of $\sigma = 3$ (Fig. 9c), shows that the estimators are very robust against the PSF radius. Here the exact and incomplete estimators are nearly identical in terms of the L_2 -distance to the true signal. The image quality improvement is about 20% for both images in terms of the L_2 -norm.

4.4 SOFI results

Figure 10 shows a comparison of using SMRE as a pre- and postprocessor for SOFI and the SOFI image without SMRE on the experimental dataset described in Sec. 4.1. Because of the much better performance all results were calculated using the ICD variant of Dykstra's projection algorithm. In fact, it is the only



(a) FRC for simulated data and corresponding reconstruction with $\sigma_{\text{PSF}} = 4$ px, $\sigma = 1$. Note that both variants of Dykstra's algorithm produce nearly identical results.



(b) Robustness against noise level with fixed PSF radius of $\sigma_{\text{PSF}} = 4$ px.

(c) Robustness against PSF radius with fixed noise level $\sigma = 3$.

Figure 9: (a) Fourier ring correlation for the images from Fig. 6. Robustness against noise strength σ (b) and PSF radius σ_{PSF} (c), based on the L_2 -error $\|\hat{x} - x^*\|_2$ of the reconstruction \hat{x} with respect to the true signal x^* normalized by the L_2 -error $\|I - x^*\|_2$ of the simulated image I with varying σ ((b)) or σ_{PSF} ((c)) for the Lena test image. The exact implementation uses a maximum multi-resolution depth $L_{\text{SMRE}} = 32$ in (a) and $L_{\text{SMRE}} = 15$ in (b) and (c).

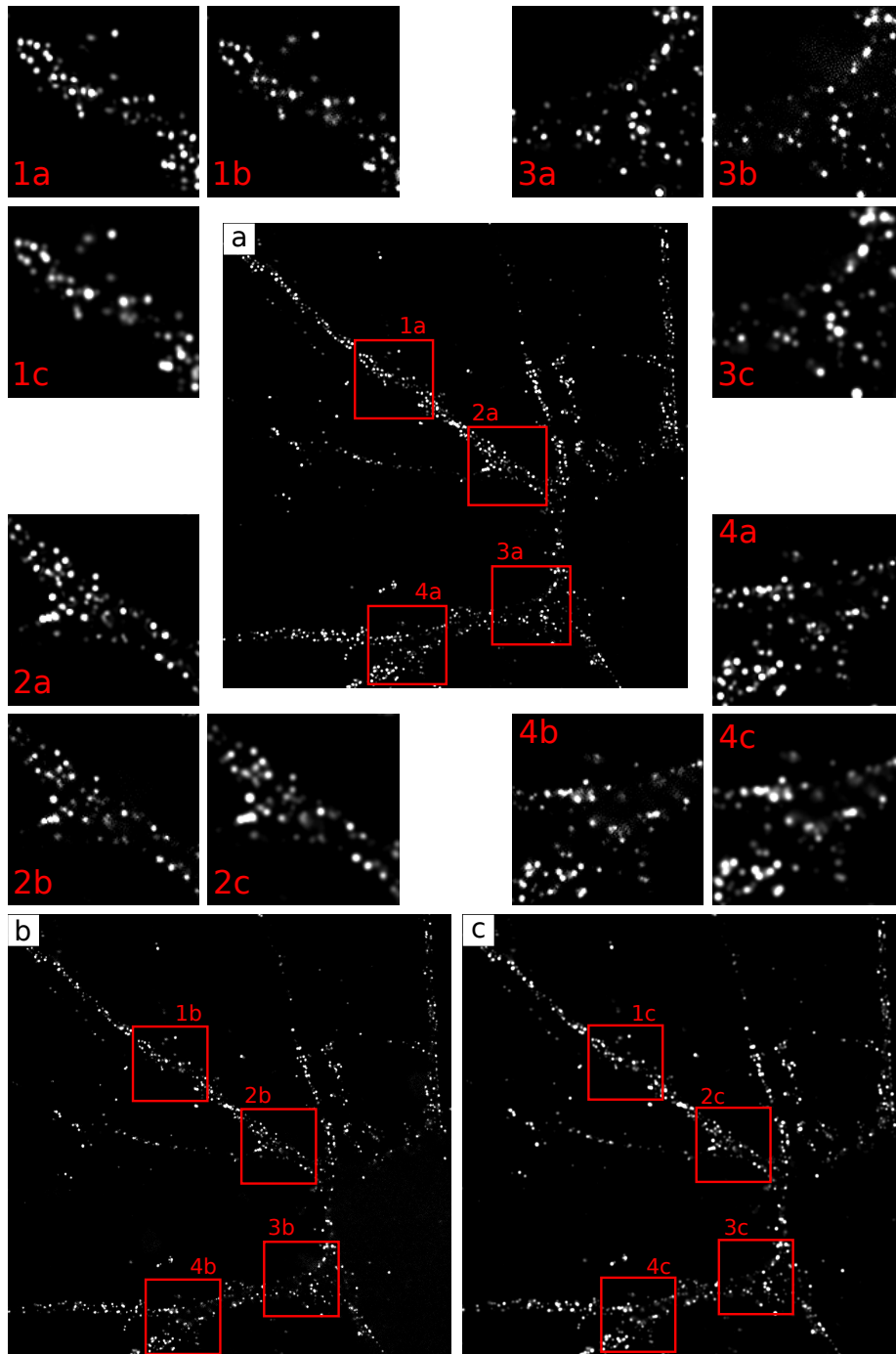
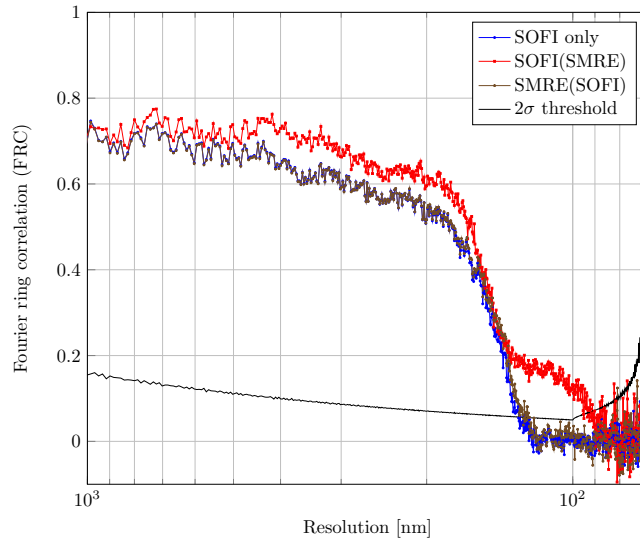
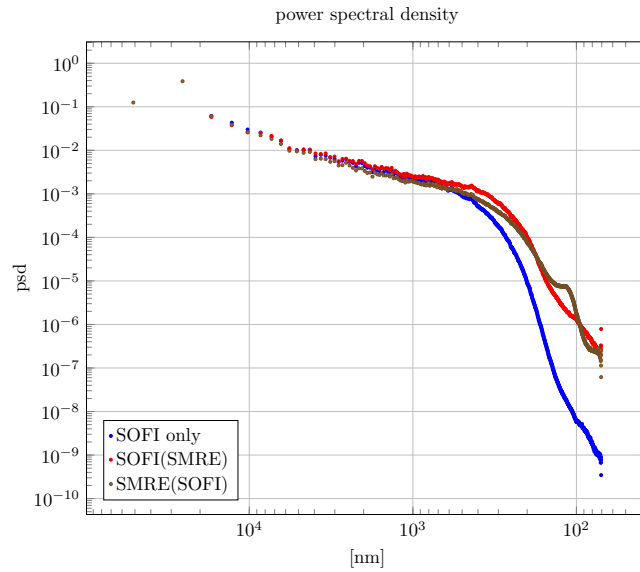


Figure 10: (a) SOFI second order with SMRE as preprocessor on each raw image, (b) SMRE applied as postprocessor on the final SOFI second order image, (c) SOFI second order. The labels of the enlarged insets correspond to the region and reconstruction method respectively. As SMRE method we use ICD.



(a) Mean FRC: The resolution is 129 nm for the SOFI result, 95 nm for SOFI with prior SMRE, and 127 nm for SMRE with prior SOFI.



(b) Normalized power spectral densities

Figure 11: Fourier ring correlation and power spectral density for the images in Fig. 10. The resolution in the result with prior (SOFI₂(SMRE)) or posterior deconvolution (SMRE(SOFI₂)) is better compared to the resolution without SMRE.

variant for which these computations are feasible. Due to the structure of the expected signal we use the generic L_2 norm as regularization.

In the following we denote by $\text{SOFI}_2(\text{ICD})$ the usage of the ICD variant of the SMRE as a preprocessor on each frame and by $\text{ICD}(\text{SOFI}_2)$ the usage of SMRE as a postprocessor on the final SOFI image of second order. If we rather want to stress that we use SMRE at all, we write $\text{SOFI}_2(\text{SMRE})$ or $\text{SMRE}(\text{SOFI}_2)$, respectively.

The comparison of $\text{SOFI}_2(\text{ICD})$ with $\text{ICD}(\text{SOFI}_2)$ and SOFI without pre- or postprocessor in Fig. 10 shows a resolution improvement by using SMRE as a preprocessor for SOFI_2 . This leads to a greatly increased numerical effort, compared to SOFI_2 and $\text{ICD}(\text{SOFI}_2)$. For $\text{ICD}(\text{SOFI}_2)$ the workload shrinks from executing SMRE on several thousand frames to applying the SMRE concept to only one, i.e. the final, image. The FRC and the power spectral density (PSD) shown in Fig. 11 suggest a resolution improvement of about 35% for $\text{SOFI}_2(\text{ICD})$. The resolution is estimated as intersection of the correlation curve with the 2σ threshold. The resolution is 129 nm for the SOFI_2 result, 95 nm for SOFI_2 with prior SMRE, and 127 nm for SMRE with prior SOFI_2 . The FRC and PSD curves in Fig. 11 are averages over several realizations of the reconstructions. The SOFI images were calculated from 1000 frames randomly chosen from the full data set. Both methods indicate that the resolution in the result with prior SMRE is the highest.

5 Discussion

We evaluated the performance of two different CUDA-implementations of Dykstra’s algorithm. The exact variant implements Dykstra’s algorithm as defined in the mathematical literature with adaptations to the CUDA architecture while the incomplete variant only computes an approximation to Dykstra’s projection by restricting the possible subsets. In numerical comparisons this approximation seems to introduce only a small error. The result is nearly as good as the exact calculation while being much faster.

For the incomplete variant a rigorous proof of the convergence of the ADMM is still missing, but the numerical evidence for the convergence is encouraging.

The exact implementation has significant disadvantages in terms of efficiency compared to the incomplete implementation. While the algorithm generally achieves good efficiency and populates all the multiprocessors, it is limited by the bandwidth of the PCIe bus, as data has to be constantly transferred between device and host. The memory transfers are necessary, because with increasing image size L_I and multi-resolution depth K_{SMRE} the total amount of memory required for storing all q_s variables easily exceeds the global memory available on the device. In that sense, the exact method cannot be implemented in a GPU-only fashion.

The usability of our SMRE approach in cooperation with super-resolution optical fluctuation imaging was shown with different datasets. Quite similar SMRE methods were deployed on images obtained from STED microscopy (Hell 2007; Frick, Marnitz, and Munk 2013).

However, using SMRE for large-scale, high-throughput applications, e.g. as preprocessor in the SOFI method, is only feasible with the incomplete variant of Dykstra’s algorithm which we have introduced in this paper. The resolution

improvements are in line with those obtained from Fourier-reweighted SOFI images where the deconvolution is done in frequency space.

The lesson to be learned from the success of the ICD is that the most crucial feature is the way the set of possible subsets is sampled. A similar problem arises in Monte Carlo simulations of e.g. protein folding or multi-dimensional spin systems. Typically the number of possible states of the system grows (for practical purposes) exponentially with the system size and thus is impossible to be completely enumerated. Instead Monte Carlo methods rely on a clever sampling of the state space by using the appropriate probability distribution, which depends on the chosen algorithm. For Metropolis-Hastings (Metropolis et al. 1953) it is the Boltzmann distribution and for the Wang-Landau (Wang and Landau 2001) or umbrella sampling it is the density of states, although it has to be constructed iteratively during the course of the simulation. With that in mind the positive results of the incomplete variant of Dykstra’s algorithm is much less surprising. Given the fact that we only used the most obvious choice of a CUDA-friendly restriction of the shapes of the subsets we expect further speedups just by revisiting the way we have partitioned an image.

There are certainly other aspects we still have to address in order to get a complete picture of the advantages and disadvantages of our statistical multi-resolution estimator and which we either had to omit or could touch only briefly in this paper. From a technical point of view one still has to investigate the influence of the choice and maximum size of the subsets and the relationship of the termination criteria of the ADMM and Dykstra iterations to the quality of the reconstructed image. The SOFI method is only one way of super-resolution microscopy and is mostly applied to widefield images. It is certainly of interest whether SMRE can be combined with other microscopy techniques, especially the parallel array microscope (PAM) (Heintzmann et al. 2001; De Beule et al. 2011), which provides high-speed, high-throughput confocal imaging. The SMRE algorithm is not restricted to 2D images. Therefore, a very interesting extension of the method would be to use 3D subsets for true 3D reconstructions. Beyond all of these technical issues we would also like to test the performance of SMRE on other physical problems. For instance, deconvolution is an important topic in the context of fluorescence lifetime microscopy (Verveer, Squire, and Bastiaens 2001) which is highly important for imaging “single molecules in action”. The fluorescence lifetime crucially depends on the details of the chemical environment of a molecule and thus is able to track subtle interactions, for instance among proteins.

Acknowledgments

We thank the Enderlein group from the III. Institute of Physics of the University of Göttingen for granting us access to their SOFI data and many fruitful discussions. In particular we enjoyed an intensive collaboration with Anja Huss and Simon Stein. Most of the computations were done in the Institute of Numerical and Applied Mathematics of the University of Göttingen. Without the encouraging support by Gert Lube and Jochen Schulz this would not have been possible.

References

- Banterle, Niccolò et al. (2013). “Fourier ring correlation as a resolution criterion for super-resolution microscopy”. In: *Journal of Structural Biology* 183.3, pp. 363–367. ISSN: 1047-8477. DOI: 10.1016/j.jsb.2013.05.004.
- Buck, Ian (2007). “GPU Computing with NVIDIA CUDA”. In: *ACM SIGGRAPH 2007 Courses*. SIGGRAPH '07. San Diego, California: ACM. ISBN: 978-1-4503-1823-5. DOI: 10.1145/1281500.1281647. URL: <http://doi.acm.org/10.1145/1281500.1281647>.
- Chambolle, Antonin and Pierre-Louis Lions (1997). “Image recovery via total variation minimization and related problems”. In: *Numerische Mathematik* 76.2, pp. 167–188. ISSN: 0029-599X. DOI: 10.1007/s002110050258.
- Chen, ZhiYu et al. (Aug. 2006). “Gray-level Grouping (GLG): An Automatic Method for Optimized Image Contrast Enhancement-part I: the Basic Method”. In: *Trans. Img. Proc.* 15.8, pp. 2290–2302. ISSN: 1057-7149. DOI: 10.1109/TIP.2006.875204.
- De Beule, Pieter A. A. et al. (2011). *Generation-3 programmable array microscope (PAM) with digital micro-mirror device (DMD)*. DOI: 10.1117/12.879611. URL: <http://dx.doi.org/10.1117/12.879611>.
- Dertinger, T. et al. (2009). “Fast, background-free, 3D super-resolution optical fluctuation imaging (SOFI)”. In: *Proceedings of the National Academy of Sciences* 106.52, pp. 22287–22292. DOI: 10.1073/pnas.0907866106.
- Dertinger, T. et al. (Aug. 2010). “Achieving increased resolution and more pixels with Superresolution Optical Fluctuation Imaging (SOFI)”. In: *Optics Express* 18, p. 18875. DOI: 10.1364/OE.18.018875.
- Diekmann, F. et al. (2001). “Visualization of microcalcifications by full-field digital mammography using a wavelet algorithm”. In: *International Congress Series* 1230.0. Computer Assisted Radiology and Surgery, pp. 526–530. ISSN: 0531-5131. DOI: 10.1016/S0531-5131(01)00082-6.
- Dong, Yiqiu, Michael Hintermüller, and M.Monserrat Rincon-Camacho (2011). “Automated Regularization Parameter Selection in Multi-Scale Total Variation Models for Image Restoration”. In: *Journal of Mathematical Imaging and Vision* 40.1, pp. 82–104. ISSN: 0924-9907. DOI: 10.1007/s10851-010-0248-9.
- Dykstra, Richard L. (1983). “An Algorithm for Restricted Least Squares Regression”. In: *Journal of the American Statistical Association* 78.384, pp. 837–842. DOI: 10.1080/01621459.1983.10477029.
- Facciolo, Gabriele et al. (2009). “Irregular to Regular Sampling, Denoising, and Deconvolution.” In: *Multiscale Modeling & Simulation* 7.4, pp. 1574–1608. DOI: 10.1137/080719443.
- Frick, Klaus, Philipp Marnitz, and Axel Munk (2012). “Statistical Multiresolution Danzig Estimation in Imaging: Fundamental Concepts and Algorithmic Framework”. In: *Electron.J.Stat.* 6, pp. 231–268. URL: <http://dx.doi.org/10.1214/12-EJS671>.
- (2013). “Statistical Multiresolution Estimation for Variational Imaging: With an Application in Poisson-Biophotonics”. In: *Journal of Mathematical Imaging and Vision* 46.3, pp. 370–387. ISSN: 0924-9907. DOI: 10.1007/s10851-012-0368-5.
- Gabay, Daniel and Bertrand Mercier (1976). “A dual algorithm for the solution of nonlinear variational problems via finite element approximation”. In:

- Computers & Mathematics with Applications* 2.1, pp. 17–40. ISSN: 0898-1221. DOI: 10.1016/0898-1221(76)90003-1.
- Gaffke, Norbert and Rudolf Mathar (1989). “A cyclic projection algorithm via duality”. In: *Metrika* 36.1, pp. 29–54. ISSN: 0026-1335. DOI: 10.1007/BF02614077.
- Grasmair, Markus (2009). “Locally Adaptive Total Variation Regularization”. In: *Proceedings of the Second International Conference on Scale Space and Variational Methods in Computer Vision*. SSVM '09. Springer-Verlag, pp. 331–342. ISBN: 978-3-642-02255-5. DOI: 10.1007/978-3-642-02256-2_28.
- Gustafsson, Mats G. L. (2005). “Nonlinear structured-illumination microscopy: Wide-field fluorescence imaging with theoretically unlimited resolution”. In: *Proceedings of the National Academy of Sciences of the United States of America* 102.37, pp. 13081–13086. DOI: 10.1073/pnas.0406877102.
- Heintzmann, R. et al. (2001). “A dual path programmable array microscope (PAM): simultaneous acquisition of conjugate and non-conjugate images”. In: *Journal of Microscopy* 204.2, pp. 119–135. ISSN: 1365-2818. DOI: 10.1046/j.1365-2818.2001.00945.x. URL: <http://dx.doi.org/10.1046/j.1365-2818.2001.00945.x>.
- Hell, Stefan W. (2007). “Far-Field Optical Nanoscopy”. In: *Science* 316.5828, pp. 1153–1158. DOI: 10.1126/science.1137395.
- Hell, Stefan W. and Jan Wichmann (1994). “Breaking the diffraction resolution limit by stimulated emission: stimulated-emission-depletion fluorescence microscopy”. In: *Opt. Lett.* 19.11, pp. 780–782. DOI: 10.1364/OL.19.000780.
- Hess, Samuel T., Thanu P.K. Girirajan, and Michael D. Mason (2006). “Ultra-High Resolution Imaging by Fluorescence Photoactivation Localization Microscopy”. In: *Biophysical Journal* 91.11, pp. 4258–4272. ISSN: 0006-3495. DOI: 10.1529/biophysj.106.091116.
- Hong, Mingyi and Zhi-Quan Luo (2012). *On the Linear Convergence of the Alternating Direction Method of Multipliers*. eprint: [arXiv:1208.3922](https://arxiv.org/abs/1208.3922).
- Huss, Anja et al. (2013). *SOFI of GABAB neurotransmitter receptors in hippocampal neurons elucidates intracellular receptor trafficking and assembly*. DOI: 10.1117/12.2006215.
- Kuno, M. et al. (2001). ““On”/“off” fluorescence intermittency of single semiconductor quantum dots”. In: *The Journal of Chemical Physics* 115.2, pp. 1028–1040. DOI: <http://dx.doi.org/10.1063/1.1377883>. URL: <http://scitation.aip.org/content/aip/journal/jcp/115/2/10.1063/1.1377883>.
- Metropolis, Nicholas et al. (1953). “Equation of State Calculations by Fast Computing Machines”. In: *The Journal of Chemical Physics* 21.6, pp. 1087–1092. DOI: <http://dx.doi.org/10.1063/1.1699114>. URL: <http://scitation.aip.org/content/aip/journal/jcp/21/6/10.1063/1.1699114>.
- Nieuwenhuizen, R. P. et al. (2013). “Measuring image resolution in optical nanoscopy”. In: *Nature Methods* 10 (6), pp. 557–562. DOI: 10.1038/NMETH.2448.
- NVIDIA Cooperation (2012). “NVIDIA Kepler GK110 Architecture Whitepaper”. URL: <http://www.nvidia.com/content/PDF/kepler/NVIDIA-Kepler-GK110-Architecture-Whitepaper.pdf>.

- Rodríguez, Paul (Jan. 2013). “Total Variation Regularization Algorithms for Images Corrupted with Different Noise Models: A Review”. In: *JECE* 2013, 10:10–10:10. ISSN: 2090-0147. DOI: 10.1155/2013/217021.
- Rust, MJ, M Bates, and X Zhuang (2006). “Sub-diffraction-limit imaging by stochastic optical reconstruction microscopy (STORM).” In: *Nature methods* 3.10, pp. 793–795. DOI: 10.1038/nmeth929.
- Saxton, W. O. and W. Baumeister (1982). “The correlation averaging of a regularly arranged bacterial cell envelope protein”. In: *Journal of Microscopy* 127.2, pp. 127–138. ISSN: 1365-2818. DOI: 10.1111/j.1365-2818.1982.tb00405.x.
- Tran, Nhat-Phuong et al. (2014). “Multi-stream Parallel String Matching on Kepler Architecture”. In: *Mobile, Ubiquitous, and Intelligent Computing*. Ed. by James J. (Jong Hyuk) Park et al. Vol. 274. Lecture Notes in Electrical Engineering. Springer Berlin Heidelberg, pp. 307–313. ISBN: 978-3-642-40674-4. DOI: 10.1007/978-3-642-40675-1_47.
- Verveer, P. J., A. Squire, and P. I. H. Bastiaens (2001). “Improved spatial discrimination of protein reaction states in cells by global analysis and deconvolution of fluorescence lifetime imaging microscopy data”. In: *Journal of Microscopy* 202.3, pp. 451–456. ISSN: 1365-2818. DOI: 10.1046/j.1365-2818.2001.00917.x.
- Vogel, C.R. (2002). *Computational Methods for Inverse Problems*. Frontiers in Applied Mathematics. Society for Industrial and Applied Mathematics. ISBN: 9780898715507.
- Wang, Fugao and D. P. Landau (2001). “Efficient, Multiple-Range Random Walk Algorithm to Calculate the Density of States”. In: *Phys. Rev. Lett.* 86 (10), pp. 2050–2053. DOI: 10.1103/PhysRevLett.86.2050. URL: <http://link.aps.org/doi/10.1103/PhysRevLett.86.2050>.

A CUDA arch

A.1 CUDA programming model

For the convenience of the reader we first briefly recall the CUDA-specific terms and the programming model. CUDA and OpenCL allow to harness the compute power of modern GPUs for entirely non-graphical purposes. The concepts are illustrated in Fig. 3. GPUs in their current design offer thousands (NVIDIA Cooperation 2012) of independent compute cores, each executing a thread and each with its own dedicated amount of memory, the registers. To distinguish the CPU, running the application, and the GPU executing data-parallel, compute-intensive tasks the notion of *host* (CPU) and *device* (GPU) was introduced. Depending on the exact architecture a varying number of cores on the GPU forms a *streaming multiprocessor* (SM). The SM manages memory requests and issues instructions for threads. The threads are addressed in groups of 32 threads, which is called a *warp*. In principle all threads of a warp execute the same instruction. Multiple warps form a thread block. A thread block resides on a single SM. Threads of the same thread block can exchange data via the *shared memory* of the SM. In order to process all of the input data, e.g. all pixels of an image, many thread blocks have to be started forming a so called *grid*. Data exchange between different thread blocks in a grid has to be done via the global device memory i.e. the VRAM. This communication inflicts already some latency which is hidden by a high level concurrency ("high occupancy") due to starting thousands of or more threads. The bottleneck of many CUDA applications is the PCIe connection between host and device since it limits the memory transfer. This becomes an even bigger problem if the compute node has more than one GPU.

CUDA can be considered as a proprietary extension of the C programming language to GPGPU computing by adding the necessary keywords to handle data-parallel multithreading. The API offers a way to call a kernel with specified thread block and grid dimensions which is executed on the GPU. Basically, a kernel is an ordinary function identified by the qualifier `__global__`. In the simplest case each instance of a kernel processes an independent data element per computation. The data element corresponding to a given thread, which has been started upon kernel launch, can be calculated from the thread's position in the grid of threads by means of the built-in variables `ThreadIdx`, `BlockDim`, `BlockIdx` and `GridDim`. If threads have to frequently access the same data elements or exchange data with other threads, the shared memory of the SM can be used as a manually managed cache. Access to the shared memory is coalesced if all threads of a warp target the same cache line. Otherwise the access is serialized in as many accesses as there are cache lines addressed. Shared memory is allocated by prepending the `__shared__` qualifier to a variable in the scope of the kernel. Synchronization among threads of a thread block is done by the `__syncthreads()` method. This is especially necessary for data exchange via the shared memory.

The kernel call itself runs asynchronous to the host part of the program, this means the next instruction after the kernel launch is immediately executed. If this is e.g. a memory transfer of the results of the kernel just started, it will probably not yield the corrected results. Thus the host has to wait until the kernel finishes, this is achieved by using the `cudaDeviceSynchronize()` directive.

In some situations, as we will show in the following sections, we can make

use of this asynchronous behavior to achieve an optimal occupancy of the device. With the advent of the Kepler architecture (NVIDIA Cooperation 2012) Nvidia introduced an improved mechanism, called Hyper-Q, to handle concurrent execution of kernels and memory transfer via the use of *streams*. A CUDA stream is a sequence of operations that execute in issue-order on the GPU. Operations in different streams may run concurrently, before Hyper-Q the concurrency was limited as the CUDA streams were multiplexed into a single hardware work queue. The Kepler architecture provides 32 work queues with no inter-stream dependencies. For a recent example of using Hyper-Q see (Tran et al. 2014).

B Example parameters file

```

1 # Listing of Parameters
2 # -----
3 subsection input data
4 # path to the .tif image
5   set image           =
6 # enforces first constraint
7   set alpha1         = 1.2
8 # enforces second constraint
9   set alpha2         = 0.12
10 # Estimate of gaussian noise standard deviation.
11 # If simulate, gaussian noise will be added to the image.
12 set gaussian noise = 0
13 # intensity of regularisation
14 set regularization = 1.0
15 # stabilises first constraint
16 set rho1           = 6.192
17 # stabilises second constraint
18 set rho2           = 1.8
19 # PSF spread
20 set sigma          = 3
21 end
22
23 subsection output
24 # where should we put the output image? Will be a tiff image
25 set output image = control.tif
26 # save preliminary results of the output image
27 set control       = false
28 end
29
30
31 subsection program flow control
32 # largest patch edge length if not using small dykstra in
33 # approximation
34 set MRdepth       = 15
35 # do a small dykstra in approximation
36 set approx        = false
37 # Set maximum number of iterations
38 set maximum iterations = 10000
39 # Reporting progress in intervals of ... Iterations
40 set report interval = 1
41 # Finish when |x_r - x_{r-1}| < tolerance
42 set tolerance     = 1e-3
43 end

```

```
44
46 subsection simulate dataset from real image
   # If set to false the input is treated as real data,
48   # if true input will be treated as test image where
   # blurring and noise are added
50   set simulate = true
   # If false simulated noise has a constant seed,
52   # if true the seed is taken from the clock
   set time seed = false
54 end
```